EES Batteries

PAPER

View Article Online
View Journal | View Issue

Cite this: *EES Batteries*, 2026, **2**, 597

Silicon-hydroborate composite electrodes with high interfacial stability for NMC811/silicon solid-state batteries

Hugo Braun, [a,b] Clea Bürgel, [a,c] Edouard Quérel, [a] Arndt Remhof *[a,b] and Corsin Battaglia [a,c,d]

Received 30th September 2025,
Accepted 13th January 2026

DOI: 10.1039/d5eb00189g

rsc.li/EESBatteries

Hydroborate solid electrolytes are compatible with high-voltage $LiNi_{0.8}Mn_{0.1}Co_{0.1}O_2$ (NMC811) positive electrodes, but their integration with high-capacity negative electrodes at industry-relevant areal capacities remains a challenge. Herein, we demonstrate a zero-lithium-excess NMC811 hydroborate solid-state battery achieving a high areal capacity of 3 mAh cm^{-2} at room temperature, enabled by a 3D silicon composite negative electrode. The $Li_3(CB_{11}H_{12})_2(CB_9H_{10})$ electrolyte is kinetically sufficiently stable to keep resistance growth low at ~0.3 Ω cm^2 $h^{-0.5}$ in contact with lithiated nanosized silicon particles and carbon fibers in 3D composite electrodes, resulting in high cycling stability. While 2D silicon electrodes require an impractically high stack pressure of 50 MPa to avoid contact loss upon delithiation, we demonstrate that silicon-hydroborate 3D composite electrodes can be operated under a moderate stack pressure of 8 MPa. Our findings demonstrate the feasibility of silicon-based hydroborate solid-state batteries with industry-relevant areal capacity operated under moderate stack pressure.

Broader context

The transition to a sustainable energy system relies heavily on the development of advanced rechargeable batteries for the electrification of transport. To meet these demands, batteries must achieve higher energy density and improved safety by integrating next-generation negative electrode materials such as silicon, which offers exceptionally high capacity, natural abundance, and a low operational potential. Combining silicon with inorganic solid electrolytes has been reported to enable high-performance electrodes. However, the most used solid electrolytes such as Li_6PS_5Cl are electrochemically unstable with lithiated silicon, limiting electrode design to 2-dimensional densely packed silicon particle electrodes, which require unrealistically high stack pressure for prolonged operation. Herein, we report the excellent kinetic stability of a hydroborate solid electrolyte in contact with lithiated silicon, enabling the use of 3-dimensional composite electrodes with silicon particles embedded in an electrolyte matrix, which can be operated at moderate stack pressure. Furthermore, the high ionic conductivity and excellent stability of the hydroborate electrolyte allows room-temperature operation in full cells with high-voltage positive electrodes. By demonstrating a pathway to integrate silicon into practical solid-state battery architectures, our study highlights how materials design can address pressing global challenges. Hydroborate-based silicon solid-state batteries could contribute to lighter, longer-lasting, and safer energy storage systems.

Introduction

Lithium-ion batteries are the dominant technology for portable electronics and mobility applications, for which specific energy (Wh kg^{-1}) and energy density (Wh L^{-1}) are key performance characteristics. Achieving significant gains in these metrics requires moving beyond graphite negative electrodes to high-capacity materials such as lithium metal or silicon.[1] Lithium metal offers the highest possible specific capacity (3860 mAh g^{-1}), but its practical application remains so far limited by dendrite growth, interfacial instability, and safety concerns in both liquid-electrolyte batteries and in solid-state batteries.[1–3] Silicon represents a safer alternative, with a similarly high theoretical capacity (3600 mAh g^{-1} when lithiated to $Li_{3.75}Si$), and higher mean lithiation potential of 0.1 V *vs.* Li^+/Li, reducing the risk of dendrite formation.[1,4,5] However, the large volume changes of silicon during repeated lithiation and delithiation induce mechanical cracking and repeated solid electrolyte interphase (SEI) reformation in liquid electrolytes, leading to continuous electrolyte consumption and rapid capacity fading.[5–7] Solid-state batteries may offer a solution to these challenges by suppressing electrolyte infiltration into cracks.[8]

Considerable efforts have therefore been devoted to combining silicon negative electrodes with solid electrolytes.

[a]*Empa, Swiss Federal Laboratories for Materials Science and Technology, 8600 Dübendorf, Switzerland. E-mail: arndt.remhof@empa.ch*
[b]*Institut für Anorganische und Analytische Chemie, Albert-Ludwigs-Universität Freiburg, 79104 Freiburg, Germany*
[c]*Departement of Information Technology and Electrical Engineering, ETH Zurich, 8092 Zurich, Switzerland*
[d]*School of Engineering, Institute of Materials, EPFL, 1015 Lausanne, Switzerland*

Silicon has been tested in solid-state batteries with sulfide-based electrolytes such as argyrodite Li_6PS_5Cl,[9–13] with polymer electrolytes,[14,15] and less frequently with halide[16] or hydride[17] electrolytes. A central challenge of silicon composite electrodes with sulfide electrolytes such as Li_6PS_5Cl is their poor interfacial stability due to the reduction of Li_6PS_5Cl at low potentials that leads to the formation of Li_2S, Li_3P and LiCl.[12] Consequently, composite electrodes with silicon particles embedded in a Li_6PS_5Cl matrix (named 3D composite electrodes in the following, see Fig. 1a–c) suffer from continuous electrolyte decomposition at the silicon–electrolyte interface. This manifests in fast growth of the interface resistance at a rate of ~10 Ω cm^2 $h^{-0.5}$ (Fig. 1c) and rapid capacity fading (21% capacity retention after 100 cycles[13]).[18] The degradation is further amplified by the presence of electronically conductive carbon additives, which promote electrolyte decomposition (10% capacity retention after 100 cycles[13]).[5,12,13,19,20] In composites containing nanosized silicon particles, the high surface area exacerbates lithium consumption during SEI formation,[18] resulting in particularly low initial coulombic efficiencies of <60% and low discharge capacities, as reported for example in ref. 20. Thus, while sulfide-based 3D composite electrodes may initially achieve high areal capacities, they suffer from both poor coulombic efficiency and rapid capacity fading, preventing their use under realistic conditions.

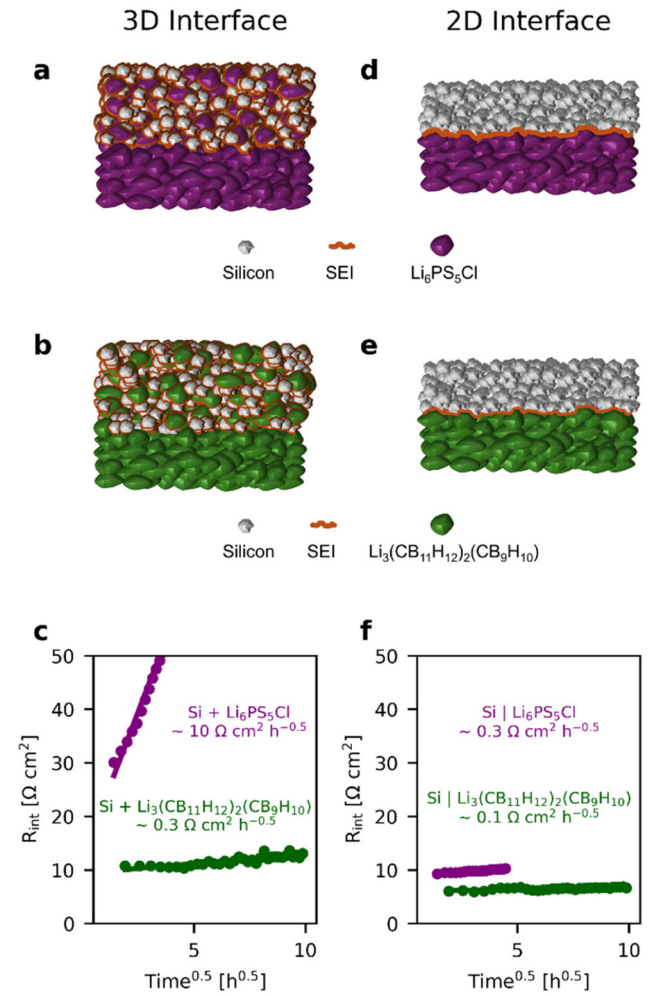

Fig. 1 (a) Schematic of a 3D composite electrode with silicon particles (light gray), Li_6PS_5Cl electrolyte particles (purple) and the SEI consisting of electrolyte reduction products (orange). (b) Corresponding schematic of a 3D composite electrode with $Li_3(CB_{11}H_{12})_2(CB_9H_{10})$ electrolyte particles (green). (c) Interface resistance growth of 3D composite electrodes with Li_6PS_5Cl electrolyte (purple, reproduced from ref. 18) and $Li_3(CB_{11}H_{12})_2(CB_9H_{10})$ electrolyte (green). (d–f) Corresponding schematics and interface resistance growth for 2D silicon electrodes. The purple datapoints in (f) are reproduced from ref. 13.

Two main strategies have emerged to address detrimental electrolyte decomposition. The first strategy is to eliminate the solid electrolyte in the silicon electrode entirely, using densely packed silicon particle electrodes, thereby reducing the silicon–electrolyte interface to a two-dimensional plane. Such electrodes (named 2D silicon electrodes in the following for simplicity, see Fig. 1d) reduce the growth of the interface resistance to a rate of ~0.3 Ω cm^2 $h^{-0.5}$ (Fig. 1f) and improve capacity retention to 58% after 100 cycles.[13] However, this strategy requires a high stack pressure ≥50 MPa to prevent contact loss in the electrode and at the electrode–electrolyte interface, a condition incompatible with practical applications.[9,12]

The second strategy is to identify alternative solid electrolytes, which do not reduce readily at low potentials, enabling 3D silicon composite electrodes without rapid electrolyte decomposition. Recent work demonstrated that a solid electrolyte consisting of $LiBH_4$ and LiI can stabilize the silicon interface and yield high initial coulombic efficiency of 96% at 60 °C.[17] However, the low room-temperature conductivity of 0.1 mS cm^{-1} renders this electrolyte unsuitable for cycling batteries with commercially relevant areal capacities of >3 mAh cm^{-2} at room temperature.[17] Furthermore, its limited oxidative stability of ~3 V *vs.* Li^+/Li prevents application in contact with high-voltage positive electrodes.[21,22]

In this work, we demonstrate that the hydroborate electrolyte $Li_3(CB_{11}H_{12})_2(CB_9H_{10})$, previously reported by some of us,[23] enables stable cycling of 3D silicon composite electrodes (Fig. 1b), even when using nano-sized silicon particles and conductive carbon additives. We observe an excellent initial coulombic efficiency of 96% and a remarkably low interface resistance growth rate of ~0.3 Ω cm^2 $h^{-0.5}$, in contrast to the rapid interface resistance growth rate ~10 Ω cm^2 $h^{-0.5}$ observed for sulfide-based electrolytes. Owing to its high room-temperature conductivity of 1.5 mS cm^{-1} and wide electrochemical stability window, $Li_3(CB_{11}H_{12})_2(CB_9H_{10})$ further enables successful integration of the 3D silicon composite electrode with a previously reported composite NMC811 electrode in a zero-lithium-excess full cell with high areal capacity of 3 mAh cm^{-2}. This cell achieves a remarkable capacity retention of 66% after 100 cycles and respectable rate capability at room temperature and 50 MPa stack pressure, while still delivering decent performance also under moderate stack pressure of 8 MPa. By establishing hydroborates as an enabling solid electrolyte class for silicon electrodes, our study

lays the foundation for competitive high-energy-density solid-state hydroborate batteries.

Results and discussion

Kinetic stability of $Li_3(CB_{11}H_{12})_2(CB_9H_{10})$ solid electrolyte in contact with lithiated silicon

Fig. 1 compares the time evolution of the interface resistance of 3D and 2D electrodes with argyrodite Li_6PS_5Cl (purple) and hydroborate $Li_3(CB_{11}H_{12})_2(CB_9H_{10})$ (green) electrolytes in contact with silicon particles after lithiation to −0.6 V *vs.* In/InLi (22 mV *vs.* Li^+/Li) (light grey). The linear behavior of the interface resistance *vs.* the square root of time is characteristic of diffusion-limited interface reactions.[24] We chose Li_6PS_5Cl as a well-established literature benchmark to study electrolyte instability against lithiated silicon. While the interface resistance of the 3D composite electrode with Li_6PS_5Cl (Fig. 1a) rises at a rate of ~10 Ω cm^2 $h^{-0.5}$ (ref. 13 and 18) as shown in Fig. 1c, the interface resistance increases at a much lower rate of only ~0.3 Ω cm^2 $h^{-0.5}$ for the 3D composite electrode with $Li_3(CB_{11}H_{12})_2(CB_9H_{10})$ (Fig. 1b). An interface resistance growth rate of ~0.3 Ω cm^2 $h^{-0.5}$ with $Li_3(CB_{11}H_{12})_2(CB_9H_{10})$ compared to ~10 Ω cm^2 $h^{-0.5}$ with Li_6PS_5Cl corresponds to roughly three orders of magnitude (1000×) longer operation time before reaching the 10 Ω cm^2 threshold for practical application.[25] It is interesting to compare this value to the values obtained for 2D electrodes (Fig. 1d–f), which are generally lower due to the lower interface area. Exemplary impedance spectra and their fits are provided in Fig. S1 and S2. Importantly, resistance growth stays low even with vapor-grown carbon fibers in the 3D composite electrode with $Li_3(CB_{11}H_{12})_2(CB_9H_{10})$ (~0.3 Ω cm^2 $h^{-0.5}$, Fig. S3). From this direct comparison between Li_6PS_5Cl and $Li_3(CB_{11}H_{12})_2(CB_9H_{10})$, we learn that hydroborate electrolytes offer considerably enhanced interfacial stability, a prerequisite for stable cycling of 3D silicon composite electrodes.

To assess the electrolyte phase stability at the silicon–electrolyte interface, X-ray diffraction (XRD) was performed on the 3D silicon–$Li_3(CB_{11}H_{12})_2(CB_9H_{10})$ composite electrodes with and without carbon fibers before and after lithiation (Fig. S4). In the case of silicon–Li_6PS_5Cl composites with carbon fibers, it was previously shown that even laboratory XRD with a standard Cu K_α X-ray source readily reveals electrolyte decomposition through additional reflections corresponding to Li_2S.[12] In contrast, for the hydroborate-based composite, the characteristic reflections of crystalline $Li_3(CB_{11}H_{12})_2(CB_9H_{10})$ are retained after lithiation, and no additional crystalline phases attributable to electrolyte reduction are detected.

Because XRD cannot exclude the presence of amorphous or nanocrystalline reaction layers, we carried out complementary X-ray photoelectron spectroscopy (XPS) analysis of the 3D silicon–$Li_3(CB_{11}H_{12})_2(CB_9H_{10})$ composite electrodes with carbon fibers before and after lithiation (Fig. S5a). We observe the expected shifts in binding energy for the Si 2p and Li 1s core-level spectra upon lithiation of the 3D silicon composite electrodes, in agreement with ref. 12, 13 and 18. Importantly, the B 1s spectrum does not shift upon lithiation of the 3D silicon composite electrode. This means that either the reduction products are not detectable by XPS, *e.g.*, because their B 1s binding environment is very similar to the pristine electrolyte, and/or that the extent of electrolyte reduction at the surface is negligible. We attribute the excellent interfacial stability of the hydroborate electrolyte to its unique chemistry: the boron clusters that constitute the anions of our electrolyte feature extended stability due to their 3D-aromatic nature.[26–28]

Additional evidence for the excellent interface stability of the 3D silicon–$Li_3(CB_{11}H_{12})_2(CB_9H_{10})$ electrode is provided by half-cell measurements *vs.* In/InLi at 60 °C. Here, we obtain an initial coulombic efficiency of 96% (Fig. 2a, dark green) similar to the best value reported for silicon electrodes in the literature which was reached with the $LiBH_4$-LiI electrolyte (red).[17] In addition, the $Li_3(CB_{11}H_{12})_2(CB_9H_{10})$ electrolyte

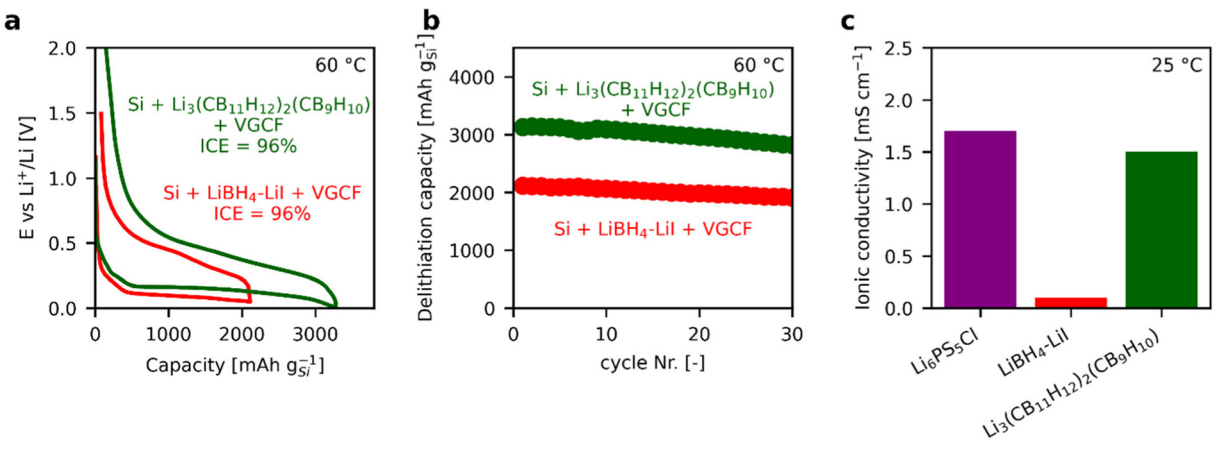

Fig. 2 (a) First-cycle potential profiles of 3D silicon composite half cells *vs.* In/InLi at 60 °C with identical current density of 0.3 mA cm^{-2} and (b) corresponding capacity retention. The data with $Li_3(CB_{11}H_{12})_2(CB_9H_{10})$ electrolyte (green) was measured in this work while the data with $LiBH_4$-LiI electrolyte (red) is reproduced from ref. 17. (c) Comparison of ionic conductivity at room temperature for Li_6PS_5Cl,[18] for $LiBH_4$-LiI,[17] and for $Li_3(CB_{11}H_{12})_2(CB_9H_{10})$.[23] All the ionic conductivity values are obtained from the corresponding literature references.

enables a higher delithiation capacity of >3100 mAh g_{Si}^{-1} (>8.9 mAh cm^{-2} at a silicon loading of 2.83 mg_{Si} cm^{-2}) with good cycling stability (Fig. 2b). Importantly, the room-temperature ionic conductivity of $Li_3(CB_{11}H_{12})_2(CB_9H_{10})$, as previously reported in ref. 23, is comparable to the reported value of fine-particle Li_6PS_5Cl,[18] allowing room-temperature cycling, which is not possible with the $LiBH_4$-LiI electrolyte due to its comparatively low room-temperature ionic conductivity of 0.1 mS cm^{-1} as reported in ref. 17 (Fig. 2c).

In summary, our results demonstrate that $Li_3(CB_{11}H_{12})_2(CB_9H_{10})$ offers not only excellent kinetic stability against reduction in silicon composites, as previously shown for $LiBH_4$-LiI,[17] but also a much higher ionic conductivity, comparable to Li_6PS_5Cl (Fig. 2c).[18] Combined with its high oxidative stability demonstrated by some of us in ref. 23, it is therefore highly suitable to enable NMC811/silicon full cells with high areal capacity at room temperature, with only one single electrolyte. The low resistance growth rate not only allows the use of 2D silicon electrodes with approximately planar interfaces but also enables the use of 3D silicon composite electrodes with large interface areas, which will be investigated in the following against NMC811 positive electrodes.

3D silicon electrodes *vs.* NMC811 electrodes in full cells with 3 mAh cm^{-2}

The silicon electrodes are characterized in a three-electrode full cell against a dry-processed NMC811 positive electrode with an areal capacity of 3 mAh cm^{-2}, and an In/InLi reference electrode (Fig. S6). Cells were cycled between a lower and upper cell cut-off voltage of 2.0 V and 4.2 V. In our previous publication, we showed that although the electrolyte exhibits limited oxidative stability up to ~3.9 V *vs.* Li^+/Li, cycling up to 4.2 V *vs.* Li^+/Li is possible with a protective coating on the NMC811 active material.[23] In the present study, we therefore deliberately limited the upper cell cut-off voltage to 4.2 V to prevent excessive electrolyte oxidation. To reach high areal capacities at room temperature without lithium plating on the silicon negative electrode, we chose a deliberately high n/p ratio of 2.7 (based on theoretical values of 3500 mAh g_{Si}^{-1} and 200 mAh g_{NMC}^{-1}). The three-electrode setup enables separate tracking of the silicon negative electrode and NMC811 positive electrode potentials, allowing us to pinpoint the origin of capacity fading and rate limitations. In contrast, the commonly used two-electrode setup with an In/InLi alloy counter electrode may give misleading results due to sluggish delithiation kinetics and larger volume changes of In/InLi compared to silicon, which alter the chemo-mechanical response of the silicon electrode.[12,13,29] The larger volume change of In/InLi compared to silicon causes an opposite pressure evolution of In/InLi *vs.* silicon half-cells compared to NMC811 *vs.* silicon full cells which was identified in ref. 13 and is confirmed in this work (Fig. S7), justifying our choice of testing in full cells. We monitored the stack pressure continuously for all the cells (Fig. S8).

Under a stack pressure of 50 MPa, both the 3D silicon composite electrode and the 2D silicon electrode enable the full cells to achieve an areal discharge capacity of around 3 mAh cm^{-2} at room temperature (Fig. 3a). Furthermore, a high capacity is retained at an elevated current density (2 mAh cm^{-2} at 1 mA cm^{-2}). The capacity retention is remarkably similar for both cells. We attribute this similar long-term cycling performance to the high stack pressure of 50 MPa, which prevents detrimental contact loss in both the 3D silicon composite electrode and the 2D silicon electrode. Furthermore, as previously shown in ref. 12 and 13, lithiated silicon has sufficient ionic and electronic conductivity such that composite architectures with electrolyte and carbon additives are not necessary, provided that the stack pressure is sufficiently high to prevent contact loss. Under a high stack pressure of 50 MPa, the capacity fading in our cells is dominated by resistance growth in the NMC811-hydroborate composite positive electrode, which is shown in Fig. S9a and S9b, while the overpotential growth at the silicon negative electrode remains minor. Therefore, the long-term cycling performance in the NMC811/silicon cells with the 3D silicon composite electrode and with the 2D silicon electrode under high stack pressure of 50 MPa is very similar. The capacity retention of 66% after 100 cycles surpasses previously reported values for Li_6PS_5Cl-based silicon composite full cells under similar cycling conditions (58%).[13] We deliberately chose long-term cycling at a relatively low current density of 0.3 mA cm^{-2}, because we expect ageing due to volume changes to be more pronounced at low current densities. The degree of (de-)lithiation of silicon is higher at lower current density, causing more volume change and faster mechanical degradation. This is also apparent in ref. 12 under 50 MPa of stack pressure, where more than 10% capacity loss is observed after 100 cycles at 0.1C, whereas virtually no capacity loss is observed after 100 cycles at 1C.[12]

The initial coulombic efficiency of the full cell improves from 70% for the 2D silicon electrode to 76% for the 3D silicon composite electrode (Fig. 3b). The three-electrode measurement reveals that the end of discharge is prematurely triggered by the abrupt rise in potential of the 2D silicon electrode (blue curve in Fig. 3c), while the 3D silicon composite electrode can be sufficiently delithiated such that the drop in potential of the NMC811 electrode triggers the end of discharge in this case (green curve in Fig. 3c). This improvement in initial coulombic efficiency translates to a capacity gain of ~0.2 mAh cm^{-2} maintained over 100 cycles. Fig. 3d uncovers that the rate capability is limited by the overpotential originating from the NMC811-hydroborate composite positive electrodes, whereas the overpotential of the negative electrodes at 1.0 mA cm^{-2} is only slightly higher than at 0.3 mA cm^{-2}. In summary, both the 3D silicon-hydroborate composite electrode and the 2D silicon electrode perform similarly well under a stack pressure of 50 MPa.

Towards moderate stack pressure

While the cell performance under 50 MPa is promising, lower stack pressures are required for practical solid-state battery applications. Under a moderate pressure of 8 MPa, the 3D silicon composite electrode (Fig. 4, light green) still delivers a

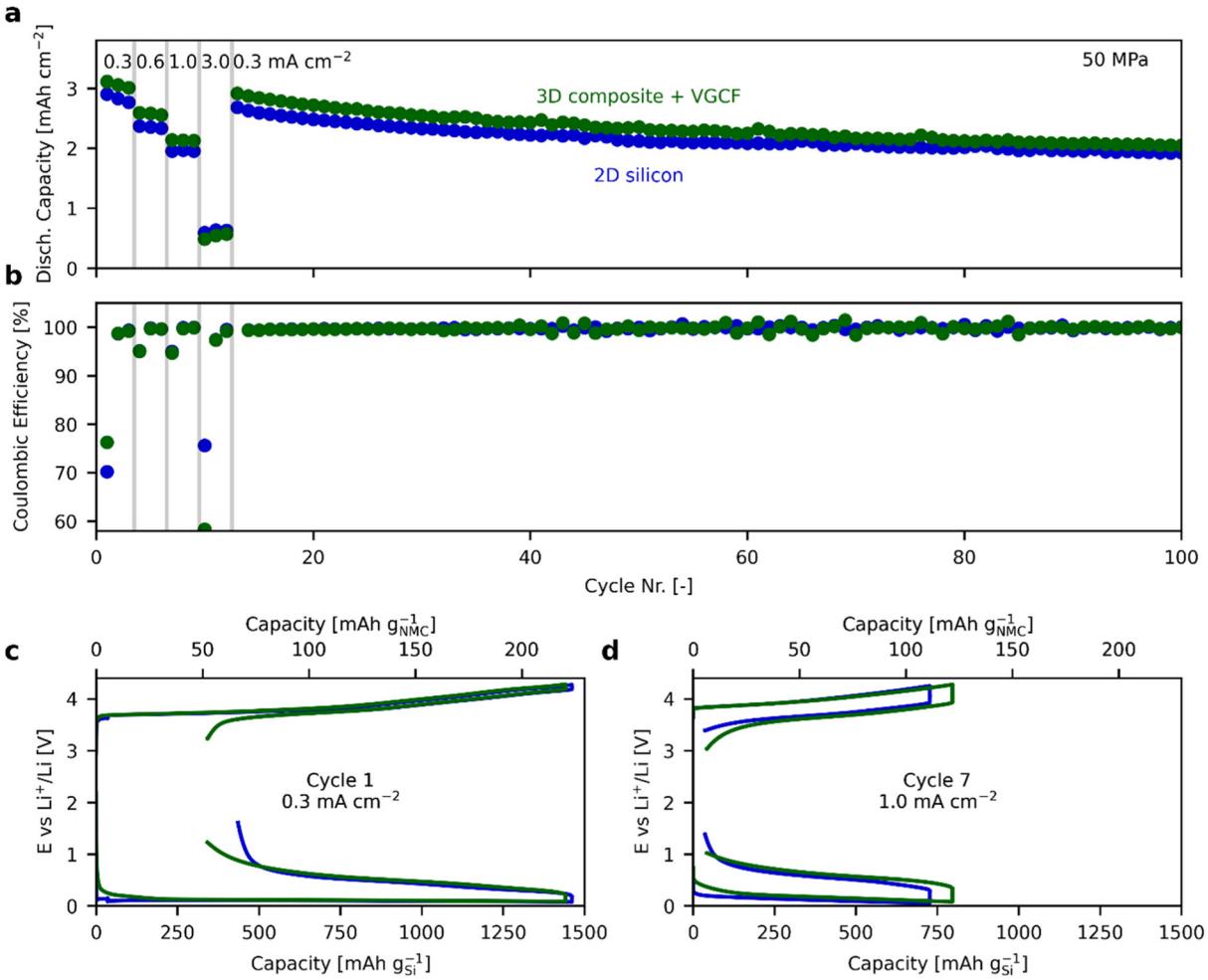

Fig. 3 (a) Discharge capacity and (b) coulombic efficiency of solid-state cells with NMC811 positive electrode and 3D silicon composite with vapor-grown carbon fibers (green) or 2D silicon (blue) negative electrode, cycled under 50 MPa stack pressure at 25 °C. (c and d) Individual potential profiles of the NMC811 positive electrode and the silicon negative electrode in the first cycle and in the seventh cycle measured in three-electrode full cells with an In/InLi reference electrode.

high first-cycle discharge capacity of 2.8 mAh cm^{-2}, high initial coulombic efficiency of 70%, and promising capacity retention (55% after 50 cycles). We confirm the excellent capacity retention achieving ~50% after 100 cycles with a 3D silicon composite electrode under 8 MPa pressure (Fig. S10). In contrast, the cell with 2D silicon electrode (light blue) displays a first-cycle discharge capacity of only 2.0 mAh cm^{-2}, low initial coulombic efficiency of 60%, and rapid capacity fading (<20% retention after 50 cycles). Unlike all the cells under a stack pressure of 50 MPa, for which capacity fading is dominated by the NMC811 positive electrode, capacity fading under a stack pressure of 8 MPa in the 2D silicon electrode case is dominated by the silicon electrode (Fig. S9c). For the 3D composite electrode under 8 MPa stack pressure, the capacity fading is not clearly dominated by either electrode (Fig. S9d). Furthermore, for the 2D silicon electrode, signs of an electronic short-circuit are visible already at 0.6 mA cm^{-2}, as indicated by the noisy charge profile in Fig. 4d. We attribute the electronic short-circuit to lithium metal plating and subsequent dendrite formation when the potential of the silicon electrode drops below 0 V *vs.* Li$^+$/Li. In 3D silicon composite electrodes, the same behavior occurs at lower silicon active material loading, resulting in a higher degree of lithiation and consequently lower electrode potential, and higher current density of 1.0 mA cm^{-2} (Fig. S11).

In summary, 50 MPa is sufficient to prevent capacity fading due to the silicon negative electrode. Under a stack pressure of 8 MPa however, capacity fading in the cells with 2D silicon electrodes is dominated by the silicon electrode, resulting in rapid capacity fading, while the cells with 3D silicon composite electrodes maintain a high capacity and decent rate performance.

The mechanics of cycling: morphological insights into electrode stability

To understand the underlying cause of the different electrochemical behaviors observed in 2D silicon electrodes and 3D silicon-hydroborate composite electrodes, we performed post-

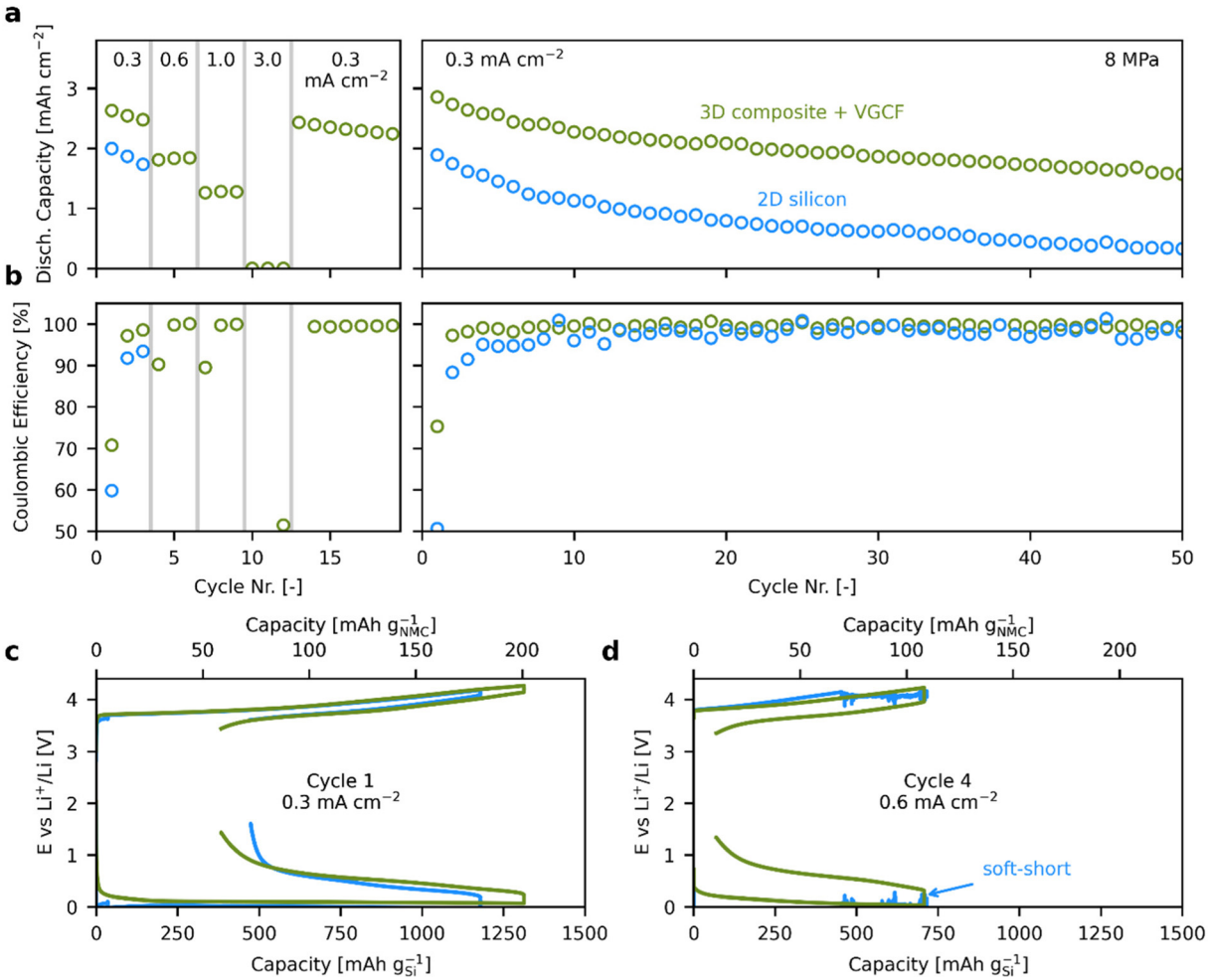

Fig. 4 (a) Discharge capacity and (b) coulombic efficiency of solid-state cells with NMC811 positive electrode and 3D silicon composite (light green) or 2D silicon (light blue) negative electrode, cycled under 8 MPa stack pressure at 25 °C. (c and d) Individual potential profiles of the NMC811 positive electrode and the silicon negative electrode in the first cycle and in the fourth cycle, measured in three-electrode full cells with an In/InLi reference electrode.

mortem *ex situ* scanning electron microscopy to examine electrode morphology after cycling.

In case of the 2D silicon electrode cycled under 50 MPa stack pressure, a network of vertical, mud-crack-like fractures is observed in the delithiated state (Fig. 5a and b). These cracks separate distinct silicon domains and are attributed to horizontal biaxial tensile stress arising during delithiation.[8] The domain size (~50 μm) observed in our study with nano-sized silicon particles is consistent with previous reports[8] and the observed cracking pattern aligns with that commonly seen in electrodes containing micron-sized silicon particles.[12,13]

In contrast, the 3D silicon composite electrode cycled under the same pressure (50 MPa) does not exhibit prominent vertical fractures at the micron scale (Fig. 5c and d). The absence of large-scale cracking can be explained by two factors. First, the 3D composite electrode contains a reduced silicon content, 38 vol% compared to ~100 vol% for the 2D silicon electrode after lithiation and compaction, resulting in smaller volumetric changes relative to the total electrode volume during cycling. This volume fraction is estimated using reported densities of 2.33, 1.1, and 1.9 g cm^{-3} for silicon, hydroborate electrolyte, and carbon fibers, respectively.[23] Second, the hydroborate electrolyte possesses a relatively low Young's modulus of typically 10–15 GPa,[30,31] compared to values for silicon of 130–190 GPa (depending on crystallographic orientation), which decrease to ~40 GPa upon full lithiation.[32] Thus, the softer hydroborate tends to deform more readily under pressure than the harder silicon, homogenizing the stress distribution in the electrode and facilitating the closing of cracks or porosity generated during cycling.

When the stack pressure is reduced to 8 MPa, vertical fractures appear upon delithiation even in the 3D silicon composite electrode shown in Fig. 5e. These cracks are oriented parallel to the direction of charge transport and do not induce noticeable performance degradation: the delithiation overpotential and potential profile remain smooth and comparable to those at higher pressure (Fig. 5g), indicating preserved electrochemical contact. In contrast, the 2D silicon electrode

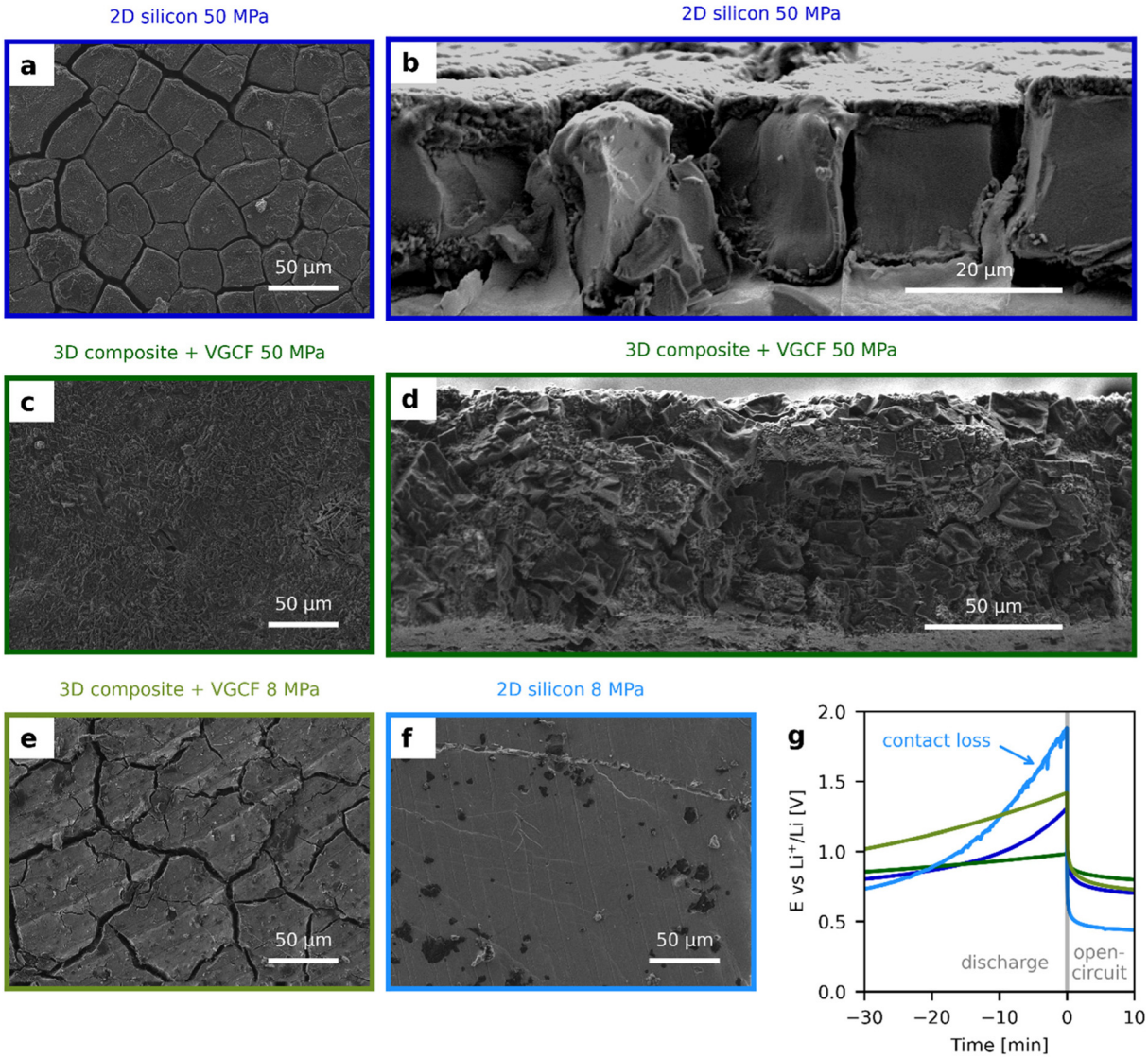

Fig. 5 Scanning electron microscopy images in top view and cross-section for (a and b) 2D silicon electrodes after cycling under 50 MPa, and for (c and d) 3D silicon composite electrodes after cycling under 50 MPa. (e) Top-view scanning electron microscopy image for 3D silicon composite electrodes after cycling under 8 MPa, and (f) corresponding image for 2D silicon electrodes after cycling under 8 MPa. (g) Exemplary potential profiles of the silicon electrodes during discharge (delithiation) and during the following open-circuit period.

cycled under 8 MPa and shown in Fig. 5f does not show vertical fractures but displays a sharp increase in delithiation overpotential and a noisy potential profile apparent in Fig. 5g, which we attribute to mechanical contact loss, potentially due to horizontal delamination. Consequently, this electrode cannot be delithiated as far as the other electrodes, as confirmed by its lower open-circuit potential after discharge shown in Fig. 5g and Fig. S12. Therefore, the electrode morphology stays compact and flat in Fig. 5f and does not feature any vertical fractures, very similar to the electrode morphology after the first lithiation and before cycling (Fig. S13).

In summary, the superior mechanical behavior of the 3D silicon composite electrodes upon delithiation is likely the main cause for their enhanced cycling performance under moderate stack pressure (8 MPa) compared to the 2D silicon electrodes. For the 3D silicon composite electrodes, a homogeneous distribution of silicon particles is beneficial,[18] suggesting that further improvements in cycling stability may be achieved through more uniform mixing, *e.g.* by ball-milling the composites. To observe the extent and mechanism of crack formation under different pressures, future studies should employ *operando* imaging techniques such as X-ray computed tomography.[8,33] These results demonstrate that 3D silicon composite electrodes offer clear advantages over 2D silicon electrodes at moderate stack pressure. From an electrochemical perspective, these 3D composite electrodes with nano-sized silicon particles and carbon additives are only viable with a sufficiently stable electrolyte, such as $Li_3(CB_{11}H_{12})_2(CB_9H_{10})$.

The impact of the negative electrode on cell-level specific energy and power

To assess the broader implications of our findings, we evaluate in Fig. 6 how the choice of the negative electrode affects the cell-level specific energy and power, assuming the weight of a thin (25 μm) hydroborate separator. As shown in Fig. 6a, the specific energy and power are very similar for the NMC811/silicon full cells with 2D silicon electrode (blue) and with 3D silicon composite electrode (green). This is primarily due to the low density of the hydroborate electrolyte (1.1 g cm^{-3}), enabling a cell-level specific energy of 250 Wh kg^{-1} at low discharge rates. Further improvements up to 275 Wh kg^{-1} could be reached by increasing the silicon utilization from currently 1100 mAh g_{Si}^{-1} to 3600 mAh g_{Si}^{-1} (continuous black line in Fig. 6a). The NMC811 utilization in our cell is 170 mAh g_{NMC}^{-1} at 17 mA g_{NMC}^{-1}, which is very similar to the values reported in ref. 13 and 34, and could be further improved by reducing the resistance of the positive electrode, for instance by increasing the temperature to 60 °C as in ref. 34.

Lithium metal electrodes form short-circuits during the first charge at a moderately low current density of 0.3 mA cm^{-2} when paired with a high areal capacity of the positive electrode of 3 mAh cm^{-2} (Fig. 6b). Consequently, they are not included in Fig. 6a (see also ref. 23). Similarly, graphite electrodes fail at higher currents, forming short-circuits when charged at 1.0 mA cm^{-2} (Fig. 6c) despite using a high fraction of solid electrolyte in the graphite composite, as recommended in ref. 35. Therefore, only values for current densities of 0.3 and 0.6 mA cm^{-2} are included for graphite electrodes in Fig. 6a. The In/InLi alloy electrode does not short-circuit (Fig. 6d), but the corresponding cells are limited to below 100 Wh kg^{-1} due

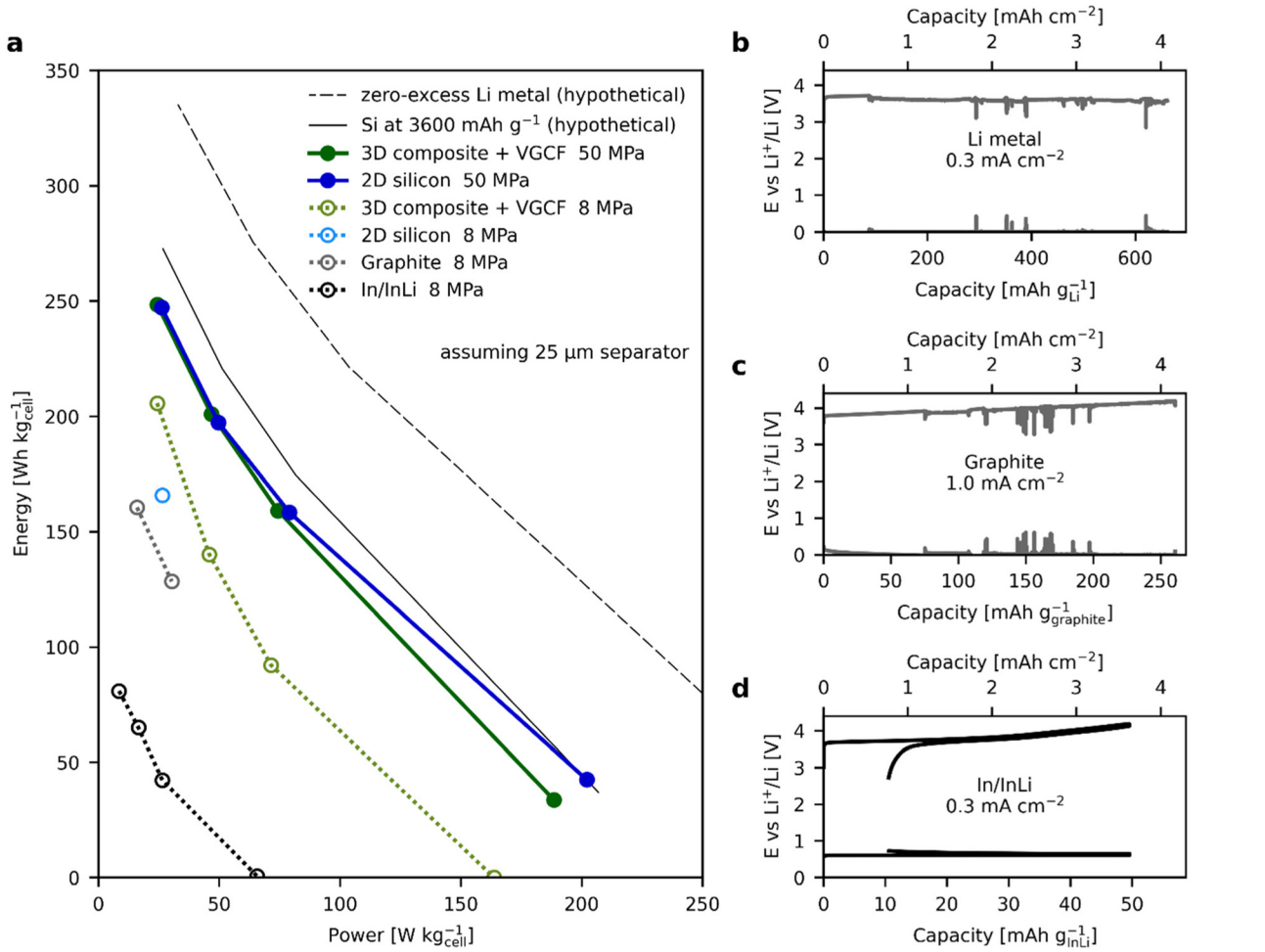

Fig. 6 (a) Ragone plot showing the cell-level specific energy and power for the solid-state batteries discussed in this work, calculated from the discharge cell voltage profiles, assuming double-side utilization of the current collectors and assuming the weight of a thin (25 μm) separator. The hypothetical lithium metal zero-excess electrode (thin dashed line) is calculated from the NMC811 positive electrode potential profile of the full cell with 3D silicon composite electrode under 50 MPa (green), but assuming zero weight of the negative electrode and a constant negative electrode potential of 0 V *vs.* Li^+/Li. Similarly, the thin solid line is calculated from the cell voltage profile of the full cell with 3D silicon composite electrode under 50 MPa (green), but assuming the weight of a 2D silicon electrode at active material utilization of 3600 mAh g_{Si}^{-1} at 0.3 mA cm^{-2}. (b–d) Potential profiles of hydroborate solid-state cells with 3 mAh cm^{-2} NMC811 positive electrode and lithium metal, graphite, or In/InLi alloy negative electrode.

to the penalty on cell voltage resulting from the high potential of In/InLi electrodes of 0.622 V *vs.* Li^+/Li and the weight of In.

In summary, silicon negative electrodes enable high areal capacity and outperform lithium metal and graphite negative electrodes in terms of rate capability as they prevent lithium metal dendrite formation at current densities where lithium plating takes place on graphite.

Fig. S14 and Table S1 compare our hydroborate solid-state battery (with NMC811 and 3D silicon composite electrodes, cycled under 50 MPa) to recently reported solid-state batteries with Li_6PS_5Cl,[12,13] polymer,[34] and halide[36] electrolytes. Our specific energy is about 30% lower than for the best-performing silicon-based cells reported in literature. This is largely due to a ~20% lower active material loading of 18.4 *vs.* 21.5–25 mg_{NMC} cm^{-2} [12,13] and increased resistance from electrolyte oxidation in the hydroborate-NMC811 composite.[23] Despite these limitations, our result clearly demonstrates the viability of silicon electrodes for competitive hydroborate solid-state batteries. It is worth noticing that the cells in this work utilize one single electrolyte in both negative and positive electrode composites and as the separator layer, facilitating manufacturing compared to cells utilizing several electrolytes such as *e.g.* halide-argyrodite bilayers.[36]

Conclusions

To conclude, we have demonstrated the integration of $Li_3(CB_{11}H_{12})_2(CB_9H_{10})$ into 3D silicon composite negative electrodes for a zero-lithium-excess NMC811 hydroborate solid-state battery. The interface resistance growth in the 3D silicon-hydroborate composite electrodes is much slower at ~0.3 Ω cm^2 $h^{-0.5}$ compared to 3D silicon–Li_6PS_5Cl composites, where interface resistance increases at ~10 Ω cm^2 $h^{-0.5}$ under similar stack pressure conditions. The kinetic stability of the $Li_3(CB_{11}H_{12})_2(CB_9H_{10})$ electrolyte enables the use of nano-sized silicon particles and carbon additives in the 3D composite electrodes. These 3D silicon-hydroborate nanocomposite electrodes can be operated reliably under moderate pressure of 8 MPa, setting them apart from Li_6PS_5Cl-based silicon electrodes, and marking an important step towards silicon solid-state batteries cycled under application-relevant stack pressures. In summary, the excellent compatibility with silicon enabled us to demonstrate hydroborate solid-state batteries with industry-relevant areal capacity (3 mAh cm^{-2}) at room temperature. Future research should focus on developing thin, robust separator layers with high lithium-ion conductivity and on optimizing the NMC811 positive electrode microstructure to enhance lithium transport.

Experimental

Solid electrolyte preparation

Hydrated $LiCB_{11}H_{12}{\cdot}xH_2O$ (KatChem) and $LiCB_9H_{10}{\cdot}xH_2O$ (KatChem) were dried under vacuum (10^{-3} mbar) at 180 °C and 230 °C for 12 h, respectively. $Li_3(CB_{11}H_{12})_2(CB_9H_{10})$ was prepared by ball milling of dried $LiCB_{11}H_{12}$ and $LiCB_9H_{10}$ in a molar ratio of 2 : 1 in argon for 4 × 15 min in a sample-to-ball weight ratio of 1 : 40 using a Spex 8000M shaker mill.

Silicon electrode preparation

All electrode preparation was carried out in an argon-filled glovebox (MBraun, H_2O and O_2 < 0.1 ppm) unless stated otherwise. Silicon nanoparticles (Si, purity > 99.9%, particle size 15 nm, type B, ACS Material) were used as received. For the 3D silicon composite electrodes with vapor-grown carbon fibers, silicon nanoparticles, $Li_3(CB_{11}H_{12})_2(CB_9H_{10})$ electrolyte and vapor-grown carbon fibers (Sigma Aldrich 719781), dried at 120 °C under vacuum for 5 h, were mixed in a weight ratio of 6 : 4 : 1 with mortar and pestle for 10 min. The 3D silicon composite electrodes without carbon fibers were prepared analogously in a weight ratio of 6 : 4.

Graphite electrode preparation

Graphite electrodes were prepared by mixing natural graphite (-325 mesh, Alfa Aesar 43209) with $Li_3(CB_{11}H_{12})_2(CB_9H_{10})$ electrolyte in a 1 : 1 weight ratio (corresponds to 30 : 70 volume ratio) with mortar and pestle for 10 min.

In/InLi electrode preparation

In/InLi counter electrodes were fabricated by pressing indium foil (>99.995%, 0.1 mm in thickness, Sigma Aldrich) and rolled-out lithium foil (purity 99.9%, 0.75 mm in thickness before rolling out, Alfa Aesar) together under 160 MPa for 3 min during cell assembly. The weight ratio of indium to lithium was chosen such that a molar ratio of 30–40 at% lithium in the In/InLi alloy is achieved.

NMC811 electrode preparation

$LiNi_{0.8}Mn_{0.1}Co_{0.1}O_2$ (NMC811) was synthesized as described by Bizzotto *et al.*[37] The NMC811 was then coated with TiO_2 and Li_2CO_3. To do so, 5 g of NMC811 were dispersed in 4 ml of a solution of titanium ethoxide (Sigma Aldrich 86710, ≤3% tetraisopropyl orthotitanate) and lithium ethoxide (Sigma Aldrich 400246, 1.0 M in ethanol) in absolute ethanol (Sigma Aldrich, 99.8%). The ethanol was pre-dried with molecular sieves. The volume was adapted to the precise amount of NMC811 to be coated, targeting a concentration of 0.6 mol% titanium and 0.6 mol% lithium in relation to the final product NMC811. Typically, a concentration of 75 μmol_{Ti} ml_{EtOH}^{-1} was obtained. Afterwards, the 50 ml round bottom flask was sealed and removed from the argon-filled glovebox. To get a homogeneous dispersion, the round bottom flask was sonicated in a sonication bath for 5 min. The round bottom flask was mounted to a rotary evaporator (Büchi) and immersed in a sonication bath for 90 min at 140 rpm while the pressure was reduced stepwise to 600 mbar, 120 mbar and 10 mbar to evaporate the ethanol. The resulting powder was then ground in an agate mortar, transferred into an alumina crucible, and calcined in a furnace for 5 h at 500 °C in air. The NMC811 coating contains titanium oxide and lithium carbonate, which help to passivate the inter-

face between the NMC811 and the electrolyte.[37,38] Subsequently, the powder was sieved to eliminate particles larger than 75 μm. Coated NMC811, $Li_3(CB_{11}H_{12})_2(CB_9H_{10})$ electrolyte and vapor-grown carbon fibers (Sigma Aldrich 719781), dried at 120 °C under vacuum for 5 h, were then mixed in a weight ratio of 70 : 23 : 05 with mortar and pestle for 10 min. 2 wt% of polytetrafluoroethylene powder (Goodfellow FP30-PD-000110) was added and fibrillated by hand in a mortar and pestle heated to 60 °C. The resulting flakes were then crushed to a powder in a laboratory mixer (IKA Tube Mill control) at 10 000 rpm for 3 min. 13.2 ± 0.5 mg of this powder was then laminated onto an aluminum current collector coated with a thin carbon layer (MSE Supplies BR0125) in a stainless-steel pressure tool of 8 mm diameter under uniaxial pressure of 390 MPa for 3 min, after heating the tool with the powder to 60 °C for 1 h.

Cell assembly

Cell assembly was carried out in an argon-filled glovebox (MBraun, H_2O and O_2 < 0.1 ppm). Three-electrode pressure cells were prepared as follows: first, the pre-laminated NMC811 electrode on an aluminum current collector (8 mm diameter, areal loading of 18.4 ± 0.7 mg_{NMC} cm^{-2}) was placed centrally in the pressure cell. Then, 100 ± 0.5 mg of $Li_3(CB_{11}H_{12})_2(CB_9H_{10})$ electrolyte were added and pressed under 160 MPa for 3 min. To fabricate the reference electrode, an indium ring (13 ± 0.65 mg) with an outer diameter of 11 mm and an inner diameter 10 mm was punched out from an indium foil (>99.995%, 0.1 mm in thickness, Sigma Aldrich) and a lithium ring (0.4 ± 0.1 mg) with identical dimensions was punched out from a rolled-out lithium foil (purity 99.9%, 0.75 mm in thickness before rolling out, Alfa Aesar). The rings were attached to the middle part of the pressure cell to serve as the In/InLi reference electrode. A schematic of the pressure cell is provided in Fig. S6. The middle part was then inserted into the cell. Subsequently, 20 ± 0.2 mg $Li_3(CB_{11}H_{12})_2(CB_9H_{10})$ electrolyte were inserted and pressed uniaxially under 160 MPa for 3 min. Finally, either 1.42 ± 0.14 mg silicon nanoparticles (for the 2D silicon electrodes), 2.37 ± 0.24 mg silicon composite without carbon fibers or 2.61 ± 0.26 mg silicon composite with carbon fibers (targeting an areal loading of 2.83 ± 0.28 mg_{Si} cm^{-2}) were added together with a copper foil of 8 mm diameter (>99.8%, 9 μm in thickness, MTI) and pressed uniaxially under 160 MPa for 3 min. Two-electrode half-cells were fabricated analogously with identical areal electrode loading (nominal diameter of 12.5 mm instead of 8 mm) and 100 ± 0.5 mg of $Li_3(CB_{11}H_{12})_2(CB_9H_{10})$ electrolyte as a separator as well as In/InLi counter electrodes. The cells were then exposed to an initial stack pressure of 55 ± 5 MPa or 8 ± 1 MPa in a custom-built pressure frame, as validated with force sensors. The stack pressure relaxed to approximately 50 MPa and 8 MPa, respectively, during the electrochemical testing (Fig. S8).

Electrochemical characterization

All electrochemical characterization was carried out in pressure cells in an argon-filled glovebox (MBraun, H_2O and O_2 < 0.1 ppm) using a VSP or VSP-3e multichannel potentiostat (BioLogic). Unless explicitly stated otherwise, all measurements were conducted at room temperature (25 °C). Electrochemical measurements were performed on a single cell for each condition due to the time- and resource-intensive nature of solid-state battery assembly and testing. The data shown are representative of our experience with similar cells prepared under the same conditions.

The evolution of interfacial resistance presented in Fig. 1 was measured in three-electrode pressure cells with a silicon working electrode (3D composite and 2D silicon), an In/InLi counter electrode and an In/InLi reference electrode as follows: first, the silicon working electrode was lithiated at 1.0 mA cm^{-2} up to a potential of −0.6 V *vs.* In/InLi (22 mV *vs.* Li^+/Li), with a constant potential hold at this potential until the degree of lithiation reached Li_3Si. Afterwards the cell was relaxed at open-circuit with potentiostatic electrochemical impedance spectroscopy measurements carried out from 1 MHz to 5 mHz with 10 mV amplitude every 2 hours. The impedance spectra were fitted using the impedance.py python module using the data points from 200 Hz to 5 mHz.[39]

Full cell cycling presented in Fig. 3 and 4 was performed in three-electrode pressure cells at constant current with cell voltage lower cut-off of 2.0 V and upper cut-off of 4.2 V using 3D silicon composite negative electrodes with vapor-grown carbon fibers and 2D silicon negative electrodes, In/InLi reference electrodes and NMC811 positive electrodes. After the cell voltage cut-off was reached, the cell was relaxed at open-circuit for 60 min. Subsequently, potentiostatic electrochemical impedance spectroscopy was measured from 1 MHz to 5 mHz with 10 mV amplitude, followed by another relaxation period of 30 min before the next constant-current step.

Ex situ characterization

XRD patterns were collected with copper K_α radiation (λ = 1.5418 Å) in transmission mode (Malvern Panalytical Empyrean with X'Celerator detector). A focusing mirror was employed to remove K_β radiation.

XPS measurements were carried out using a Nexsa G2 surface analysis system (Thermofisher). All the samples were transferred from the glovebox to the instrument with a vacuum transfer system. XPS spectra were acquired at room temperature using a monochromated Al Kα X-ray source ($h\nu$ = 1486.6 eV) operated at 72 W (12 kV, 6 mA). The analyzed area was an elliptical region of approximately 400 μm × 800 μm. Charge neutralization was achieved using a dual-mode flood gun (low-energy electrons and Ar^+ ions). The base pressure during analysis was typically 1 × 10^{-9} mbar. High-resolution core-level spectra were recorded with a pass energy of 20 eV (50 eV for Si 2p), step size of 0.1 eV, and dwell time of 50 ms per point. All spectral fitting was performed using CasaXPS software. Shirley-type backgrounds were subtracted from all core-level regions, and peaks were fitted using symmetric Lorentzian–Gaussian (LA(50)) line shapes. Binding energies were calibrated by referencing the carbonate C 1s peak to 289.20 eV, which was present in all samples. For intensity normalization,

spectra were normalized to the B 1s peak area of the solid electrolyte to enable comparison across samples. For the Si 2p region, since the Si signal intensity was significantly attenuated in the lithiated composite, spectra were instead normalized by setting the integrated total signal intensity to unity. For the fitting of Si 2p spectra, a doublet was used for Si^0 and singlets were used for all chemical environments (Si–O, Li–Si, Li–Si–O).

Electrodes for scanning electron microscopy were recovered from the cells after galvanostatic dis-/charge cycling. The images were taken at an accelerating voltage of 5 kV using a ZEISS Gemini SEM 460.

Author contributions

H. Braun and C. Bürgel conducted the experiments and analyzed the data. Edouard Quérel analyzed the XPS data. H. Braun, A. Remhof and C. Battaglia conceived the idea and wrote the manuscript. All authors discussed the results.

Conflicts of interest

We declare that none of the authors have competing financial or non-financial interests.

Data availability

The data supporting this work are available *via* Zenodo at https://doi.org/10.5281/zenodo.17159631

Supplementary information (SI) is available. See DOI: https://doi.org/10.1039/d5eb00189g.

References

1 D. Andre, H. Hain, P. Lamp, F. Maglia and B. Stiaszny, *J. Mater. Chem. A*, 2017, **5**, 17174–17198.
2 J. Janek and W. G. Zeier, *Nat. Energy*, 2023, **8**, 230–240.
3 M. Burton, S. Narayanan, B. Jagger, L. F. Olbrich, S. Dhir, M. Shibata, M. J. Lain, R. Astbury, N. Butcher, M. Copley, T. Kotaka, Y. Aihara and M. Pasta, *Nat. Energy*, 2025, **10**, 135–147.
4 A. Song, W. Zhang, H. Guo, L. Dong, T. Jin, C. Shen and K. Xie, *Adv. Energy Mater.*, 2023, **13**, 2301464.
5 H. Huo and J. Janek, *ACS Energy Lett.*, 2022, **7**, 4005–4016.
6 L. Wang, J. Yu, S. Li, F. Xi, W. Ma, K. Wei, J. Lu, Z. Tong, B. Liu and B. Luo, *Energy Storage Mater.*, 2024, **66**, 103243.
7 W. He, W. Xu, Z. Li, Z. Hu, J. Yang, G. Qin, W. Teng, T. Zhang, W. Zhang, Z. Sun and X. Yu, *Adv. Sci.*, 2025, **12**, 2407540.
8 D. L. Nelson, S. E. Sandoval, J. Pyo, D. Bistri, T. A. Thomas, K. A. Cavallaro, J. A. Lewis, A. S. Iyer, P. Shevchenko, C. V. Di Leo and M. T. McDowell, *ACS Energy Lett.*, 2024, **9**, 6085–6095.
9 T. Neumann, L. A. Dold, A. T. Cerny, E. Tröster, M. Günthel, A. Fischer, K. P. Birke, I. Krossing and D. Biro, *Batteries Supercaps*, 2025, **8**, e202400412.
10 S. Jing, Y. Lu, Y. Huang, H. Liu, Y. Shen, W. Kuang, H. Shen, S. Liu, Z. Zhang and F. Liu, *Adv. Mater.*, 2024, **36**, 2312305.
11 M. Rana, Y. Rudel, P. Heuer, E. Schlautmann, C. Rosenbach, M. Y. Ali, H. Wiggers, A. Bielefeld and W. G. Zeier, *ACS Energy Lett.*, 2023, **8**, 3196–3203.
12 D. H. S. Tan, Y.-T. Chen, H. Yang, W. Bao, B. Sreenarayanan, J.-M. Doux, W. Li, B. Lu, S.-Y. Ham, B. Sayahpour, J. Scharf, E. A. Wu, G. Deysher, H. E. Han, H. J. Hah, H. Jeong, J. B. Lee, Z. Chen and Y. S. Meng, *Science*, 2021, **373**, 1494–1499.
13 H. Huo, M. Jiang, Y. Bai, S. Ahmed, K. Volz, H. Hartmann, A. Henss, C. V. Singh, D. Raabe and J. Janek, *Nat. Mater.*, 2024, **23**, 543–551.
14 H. Pan, L. Wang, Y. Shi, C. Sheng, S. Yang, P. He and H. Zhou, *Nat. Commun.*, 2024, **15**, 2263.
15 P. Dong, Y. Cha, X. Zhang, J. Zamora and M.-K. Song, *ACS Appl. Mater. Interfaces*, 2024, **16**, 41018–41026.
16 H. Nagata and K. Kataoka, *J. Power Sources*, 2024, **623**, 235443.
17 Y. Huang, B. Shao, Y. Wang and F. Han, *Energy Environ. Sci.*, 2023, **16**, 1569–1580.
18 H. Huo, Y. Bai, S. L. Benz, T. Weintraut, S. Wang, A. Henss, D. Raabe and J. Janek, *Adv. Mater.*, 2024, **37**, 2415006.
19 D. Cao, T. Ji, A. Singh, S. Bak, Y. Du, X. Xiao, H. Xu, J. Zhu and H. Zhu, *Adv. Energy Mater.*, 2023, **13**, 2203969.
20 M. Grandjean, M. Perrey, X. Randrema, J. Laurier, P. Chenevier, C. Haon and S. Liatard, *J. Power Sources*, 2023, **585**, 233646.
21 D. Sveinbjörnsson, A. S. Christiansen, R. Viskinde, P. Norby and T. Vegge, *J. Electrochem. Soc.*, 2014, **161**, A1432.
22 R. Asakura, L. Duchêne, R.-S. Kühnel, A. Remhof, H. Hagemann and C. Battaglia, *ACS Appl. Energy Mater.*, 2019, **2**, 6924–6930.
23 H. Braun, R. Asakura, A. Remhof and C. Battaglia, *ACS Energy Lett.*, 2024, **9**, 707–714.
24 P. M. Attia, W. C. Chueh and S. J. Harris, *J. Electrochem. Soc.*, 2020, **167**, 090535.
25 C. D. Alt, N. U. C. B. Müller, L. M. Riegger, B. Aktekin, P. Minnmann, K. Peppler and J. Janek, *Joule*, 2024, **8**, 2755–2776.
26 J. Poater, M. Solà, C. Viñas and F. Teixidor, *Angew. Chem., Int. Ed.*, 2014, **53**, 12191–12195.
27 O. El Bakouri, D. W. Szczepanik, K. Jorner, R. Ayub, P. Bultinck, M. Solà and H. Ottosson, *J. Am. Chem. Soc.*, 2022, **144**, 8560–8575.
28 E. L. Muetterties, J. H. Balthis, Y. T. Chia, W. H. Knoth and H. C. Miller, *Inorg. Chem.*, 1964, **3**, 444–451.
29 S. Yanev, C. Heubner, K. Nikolowski, M. Partsch, H. Auer and A. Michaelis, *J. Electrochem. Soc.*, 2024, **171**, 020512.
30 J. L. Hempel, S. Thapa, K. Kim, K. E. Kweon, B. C. Wood, Y. V. Sevryugina, R. Mohtadi, O. Tutusaus and Y.-T. Cheng, *J. Power Sources*, 2025, **641**, 236800.
31 M. Brighi, F. Murgia and R. Černý, *Adv. Mater. Interfaces*, 2022, **9**, 2101254.
32 L. A. Berla, S. W. Lee, Y. Cui and W. D. Nix, *J. Power Sources*, 2015, **273**, 41–51.

33 Y. Sakka, M. Matsumoto, H. Yamashige, A. Takeuchi, M. Uesugi, K. Uesugi, C. Zhong, K. Shimoda, K.-i. Okazaki and Y. Orikasa, *J. Electrochem. Soc.*, 2024, **171**, 070536.
34 G. Homann, Q. Wang, S. Liu, A. Devincenti, P. Karanth, M. Weijers, F. M. Mulder, M. Piesins, T. Gouveia, A. Ladam, S. Fantini and C. Battaglia, *ACS Appl. Energy Mater.*, 2024, **7**, 10037–10043.
35 A. L. Davis, V. Goel, D. W. Liao, M. N. Main, E. Kazyak, J. Lee, K. Thornton and N. P. Dasgupta, *ACS Energy Lett.*, 2021, **6**, 2993–3003.
36 L. Zhou, T.-T. Zuo, C. Y. Kwok, S. Y. Kim, A. Assoud, Q. Zhang, J. Janek and L. F. Nazar, *Nat. Energy*, 2022, **7**, 83–93.
37 F. Bizzotto, W. Dachraoui, R. Grissa, W. Zhao, F. Pagani, E. Querel, R.-S. Kühnel and C. Battaglia, *Electrochim. Acta*, 2023, **462**, 142758.
38 F. Walther, F. Strauss, X. Wu, B. Mogwitz, J. Hertle, J. Sann, M. Rohnke, T. Brezesinski and J. Janek, *Chem. Mater.*, 2021, **33**, 2110–2125.
39 M. D. Murbach, B. Gerwe, N. Dawson-Elli and L.-K. Tsui, *J. Open Source Software*, 2020, **5**, 2349.